Journal of Physics D:
Applied Physics

PAPER • **OPEN ACCESS**

Stress management of large size (001) and (111) diamond wafers for quantum-optical applications

To cite this article: Jan Engels *et al* 2026 *J. Phys. D: Appl. Phys.* **59** 035307

View the article online for updates and enhancements.

You may also like

- Autler–Townes splitting in Rydberg atoms: transition dipole matrix element extraction and field efficiency analysis
Brian C Holloway, Gavin M Chase, Lee E Harrell et al.

- Enhancing pre-clinical microbeam radiation therapy capabilities at PETRA III beamline P61A through high-precision beam delivery
Malin Kügele, Vincent Tim de Rover, Abdul Hamada et al.

- ICRH modelling of DTT in full power and reduced-field plasma scenarios using full wave codes
A Cardinali, C Castaldo, F Napoli et al.

This content was downloaded from IP address 129.233.195.225 on 23/03/2026 at 15:19

IOP Publishing J. Phys. D: Appl. Phys. **59** (2026) 035307 https://doi.org/10.1088/1361-6463/ae3778

Journal of Physics D: Applied Physics

OPEN ACCESS

RECEIVED
17 November 2025

REVISED
19 December 2025

ACCEPTED FOR PUBLICATION
13 January 2026

PUBLISHED
23 January 2026

Original content from this work may be used under the terms of the Creative Commons Attribution 4.0 licence.

Any further distribution of this work must maintain attribution to the author(s) and the title of the work, journal citation and DOI.

PAPER

Stress management of large size (001) and (111) diamond wafers for quantum-optical applications

Jan Engels[1,*], Jürgen Weippert[1], Jan Kustermann[1], Sven Mägdefessel[1], Niklas Mathes[1], Jan Jeske[1], Lutz Kirste[1], Peter Knittel[1], Patricia Klar[1], Tobias Fehrenbach[2], Christoph Wild[2] and Vadim Lebedev[1]

[1] Fraunhofer Institute for Applied Solid State Physics IAF, Tullastr. 72, Freiburg, D-79108, Germany
[2] Diamond Materials GmbH, Hans-Bunte-Str. 19, Freiburg, D-79108, Germany
[*] Author to whom any correspondence should be addressed.

E-mail: jan.engels@iaf.fraunhofer.de

Keywords: diamond, CVD, stress management, defect reduction, ODMR, T_2 coherence time, NV center alignment

Abstract

Large size (001) and (111) diamond wafers are essential for various applications in quantum sensing and quantum computing. Notably, (111) diamond wafers offer the advantage of self-organized single alignment of nitrogen-vacancy (NV) centers, which are crucial for these applications. In this work, we demonstrate the near-single alignment of NV centers across the entire area of 2 inch (111) diamond wafers. However, several challenges arise during the growth process by chemical vapor deposition. When attempting to grow wafers, stress induces a curvature of the wafer. The curvature can lead to crack formation. Here, we propose solutions to prevent cracking such as cyclic growth with growth and etch steps, columnar growth, and epitaxial lateral overgrowth in two layers. We discuss hypothesis that explain why and under what circumstances these solutions are successful, providing evidence through methods such as photoluminescence mapping, Raman spectroscopy, SEM analysis, and x-ray diffraction. Interestingly, all the different growth methods reveal the same systematic characteristics of growth type, related stresses, and radii of curvature. Furthermore, measures are implemented to reduce the defect density. Optically detected magnetic resonance analysis of NV centers in our monocrystalline diamond wafers yield T_2 coherence times of 26 μs.

1. Introduction

Large size (001) and (111) diamond wafers are foundational for applications in quantum sensing and quantum computing. The (111) diamond wafers have a distinct advantage due to the self-organized single alignment of nitrogen-vacancy (NV) centers [1–3] which is crucial for quantum applications. In this work, we demonstrate the necessary stress management required to produce freestanding (001) and (111) diamond wafers. Moreover, solutions for defect reduction are implemented, which are necessary for enabling quantum applications. In this context, we highlight the enhancement of our T_2 coherence time by a factor of 2.8–26 μs on 2 inch (111) diamond wafers compared to our previous work [4, 5]. Furthermore, we delve into the near-single alignment of NV centers over the 2 inch area. These findings have significant implications for the application in quantum magnetometric sensors, which are capable of detecting sample magnetic fields in extremely short measurement times via wide field Optically detected magnetic resonance (ODMR), where the size of sample is same as the size of the wafer [6, 7]. However, challenges arise when growing on the (111) diamond surface, where tensile stress results in a concave curvature. Conversely, when growing on the (001) diamond surface, compressive stress leads to a convex curvature. Both (001) and (111) diamond wafer growth is based on the same principles: Radii of curvature in any direction can lead to cracks, compromising the integrity of the wafer during diamond growth, post-growth cooling or a potentially following lithographic process. Thus, thicknesses over 100 μm have, in most cases, been unattainable due to crack formation. However, to detach the wafer from silicon, 300 μm thick diamond wafers are necessary for its mechanical stability. To address these

© 2026 The Author(s). Published by IOP Publishing Ltd

challenges, we propose several solutions. For both (111) and (001) wafers, similar techniques such as patterned nucleation growth (PNG) directly on the initial Ir/YSZ/Si template and epitaxial lateral overgrowth (ELO) on a structured iridium film atop a diamond layer are employed [8, 9]. For simplicity, we will use the acronym ELO to refer to both types of processes, including PNG. Additionally, for (001) diamond wafers, we explore the implementation of columnar growth as well as a cyclic growth and etch technique, yielding a layered structure characterized by alternating stress signs. Here, hydrostatic tensile stress corresponds to a positive sign and compressive stress to a negative sign (table 2).

One of the ELO-techniques for (111) wafers is the manufacturing of a stack with the masks 1 and 2 in two growth heights. The fundamental concept of this method is to continue diamond growth in high-quality areas while ceasing growth in high-defect regions such as the nucleation areas. This is accomplished through a stack of two structured layers: the first layer employs the ELO method directly on the Ir/YSZ/Si template from a first ELO pattern, while the second structured layer consists of a structured iridium film atop the first diamond layer. Both structured layers are aligned to achieve the following architecture: the structured iridium film of the second layer halts diamond growth in the nucleation and coalescence regions of the first ELO pattern. This termination of defect growth in these critical areas enhances the overall diamond quality in the subsequent diamond overgrowth step.

The radius of curvature R of a wafer with a diameter D of 2 inch is calculated using the following equation, where the sagitta s is defined as equivalent to the vertical runout of the wafer:

$$R = \frac{D^2}{8s} + \frac{s}{2}.$$

So, for a critical high limit of vertical runout s of 50 μm the radius of curvature R is 6.5 m. Crack formation is likely to occur beyond this limit.

2. Experimental

ODMR measurements were performed using a custom-built transmission setup with 532 nm laser excitation and a Rohde & Schwarz SMB100B microwave (MW) source connected to a Sasaki antenna. The pulse sequences for the Ramsey and Hahn–Echo (T_2) measurements were adapted from work by Zhang *et al* [10]. For the estimation of the orientation purity (near-single alignment of NV centers), the external magnetic field—using a permanent magnet—was aligned parallel to each of the NV families individually, while for the survey in the continuous wave ODMR spectra it was intentionally not aligned with any of the potential orientations. In order to ensure equal amounts of effective MW power seen by the NV centers, the applied MW power was adjusted to result in the same Rabi frequency for all four families [6]. The wafer curvature was measured using a Surfcom 1800D (Zeiss) surface texture measuring instrument. Photoluminescence (PL) and Raman spectromicroscopy was performed using a Renishaw Invia setup with a 532 nm excitation laser with 1 mW power and x-ray diffraction was performed using high-resolution x-ray diffraction setups (HRXRD,Malvern Panalytical X'Pert Pro MRD and Rigaku Smartlab). Any Raman measurement result was averaged over a measurement plane area of at least 25 μm [2] with at least 25 measurement points. Measurements of the top measurement plane were done in a depth of 10 μm below the diamond surface; and directly on the surface in case of method 5. The diamonds were synthesized using a chemical vapor deposition [11] (CVD) process within both a 915 MHz and a 2.45 GHz ellipsoid reactor. Initially, an H-plasma treatment was applied for 13 min to prepare the substrate.

To achieve a more planar (111) and (001) growth over an area of 2 inches, we considered four main approaches:

A) Method 1: cyclic growth and etch on (001) wafers which produces nitrogen-doped layers with more than 300 μm thickness through repeated growth and etching cycles. The successful application of this method on (111) wafers has not been demonstrated yet (figure 1(a)).
B) Method 2: columnar growth on (001) wafers which forms pyramidal structures with {111} facets, where the top surfaces of each column form a pyramid with {111} facets or similar shallower pyramids, inducing tensile stress in the continuing overgrowth. This method has not been tested for (111) wafers (figure 1(b)).
C) Methods 3–4: ELO is implemented on (001) wafers using two distinct mask patterns which guide the overgrowth: the circle pattern and the net pattern (figure 1(c)).—Method 5: on (111) wafers, nominally undoped layers are first established to improve diamond quality, followed by a thin functional nitrogen-doped layer grown on patterned structures (ELO). These masks' patterns are only helpful for the (111) wafer orientation and involves ELO with patterned structures to

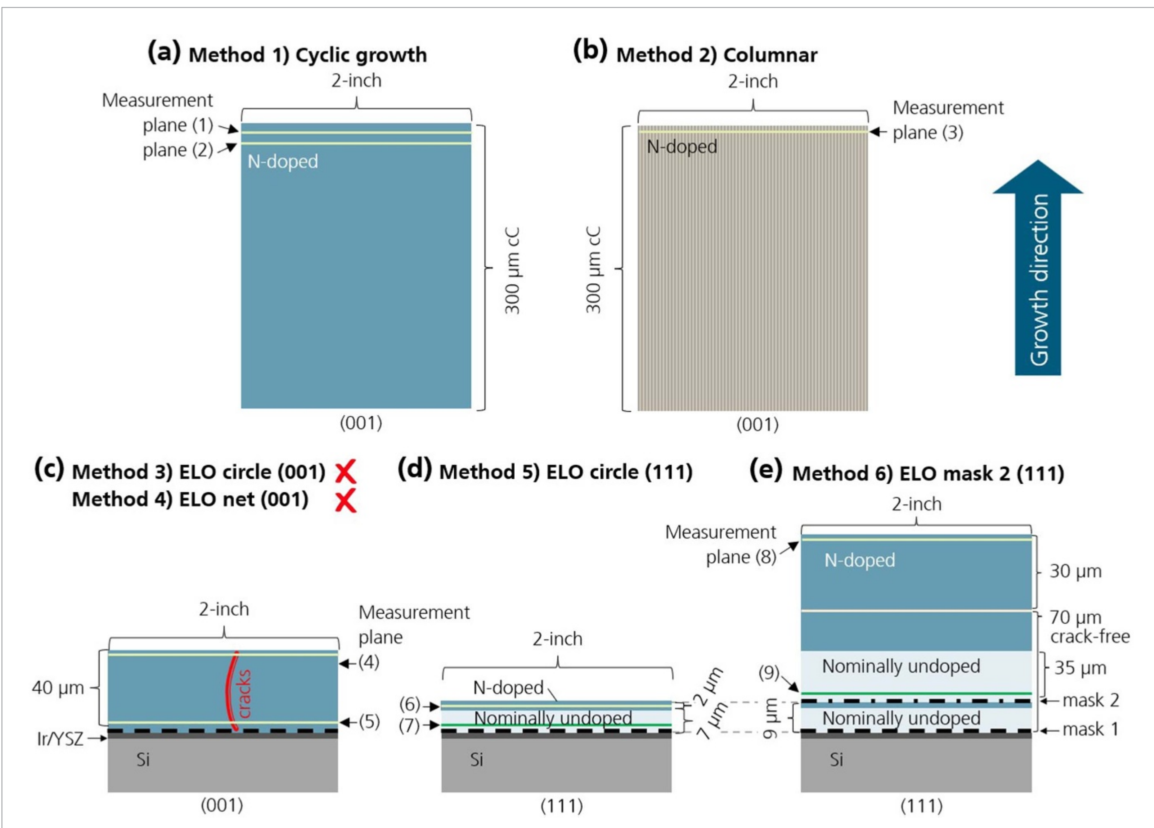

Figure 1. Diagram of the grown diamond samples with nominally undoped and nitrogen-doped layers. (a) Method 1 employs cyclic growth and etching. (b) Method 2 utilizes columnar growth of (001) wafers. The ELO methods implement lithographic masks for patterned structures: (c) in methods 3 and 4, crack formation occurs for the (001) oriented wafers. (d) In method 5, the ELO pattern is effective for producing crack-free (111) wafers. (e) In method 6, a 100 μm thick stack features two pattern layers, where mask 2 is applied during a growth height of 9 μm to enhance the diamond quality in the overgrown layer.

implement more tensile stress during diamond growth. These methods have also been largely tested for (001) wafers, and we will discuss why a positive result could not be demonstrated here (figure 1(d)).

D) Method 6: a stacked structure on (111) wafers is fabricated by combining undoped and nitrogen-doped layers with the lithographically patterned nucleation mask 1 and with the structured Ir mask 2 (figure 1(e)).

3. Growth methods and results

The growth conditions over an area of 2 inches of the above-mentioned main approaches (A–D) are summarized in (table 1). For (001) wafers, the growth conditions of the standard growth, the cyclic growth of method 1 (001), and for the growth in methods 3 and 4 are identical (figures 1 (a) and (c)).

In method 1 the process step (I) of etching is carried out using a gas mixture of oxygen and hydrogen, creating negative etching pyramids with a square base on the diamond surface (see Competing Interests section). Due to the cyclic diamond growth, the process step (II)—the only step where growth occurs—results in two layers with different material properties:

1. The horizontal layer (1) is formed when laterally growing over the pyramidal etch pits, which are approximately 1 μm in side length with their {111} facets (figure 2).
2. The horizontal layer (2) is formed when overgrowing a smooth, homogeneous (001) surface, after the etch valleys of the pyramids have been closed.

These alternating layers (1) and (2) are repeated several times to form a wafer with a thickness of 300 μm (figure 2).

For the columnar (001) wafers of method 2, the same oxygen and nitrogen content was maintained, as for the standard growth of (001) wafers, but the methane content was reduced to 1.25% (figure 1(b)). In the case of nitrogen-doped layers on the (111) wafers, the methane content was further decreased to 0.5% and the nitrogen content in the inlet gas mixture was increased to 5000 ppm

Table 1. Process parameters of each method and measurement results of the radius of curvature, performed ODMR measurements and RAMAN-, PL-, and EDX-mappings. Single RAMAN and PL measurements with 25 averaged measurement points were performed for each method, as well as REM measurements. If the absolute value of the radius of curvature is less than 6, the wafer deflection is so large that the wafer has already fractured, making further accurate data unavailable.

Method (measurement plane)	Wafer orientation	Comment	Temperature/°C	O_2/H_2/%	N_2/H_2/ppm	CH_4/H_2/%	Radius of curvature/m	Mappings/ODMR measurements
Standard growth	(001)	N-doped	840–860	0.15	3040	1.75	6	—
Nom. undoped	(111)	Nom. undoped	840–860	0.15	0	1.25	−6	—
Standard growth	(111)	N-cap	840–860	0.15	5000	0.5	−6	—
1) Cyclic (etch)	(001)	2 h: etch	840–860	2	0	0	11	—
1) Cyclic growth	(001)	1.5 h: N-doped	840–860	0.15	3040	1.75	11	—
2) Columnar	(001)	Result: oparque	<750	0.15	3040	1.25	16	—
3) ELO circle	(001)	N-doped	840–860	0.15	3040	1.75	6	RAMAN
4) ELO net	(001)	N-doped	840–860	0.15	3040	1.75	6	RAMAN, PL
5) ELO circle	(111)	Nom. undoped	840–860	0.15	0	1.25	10	RAMAN, PL, ODMR
6) ELO mask 2 (9)	(111)	Nom. undoped	840–860	0.15	0	1.25	10	RAMAN, PL, EDX
6) ELO mask 2 (8)	(111)	N-cap	840–860	0.15	5000	0.5	6.5	RAMAN, PL, ODMR

Figure 2. Schematic sketch of the concept behind the method 1 of cyclic growth and etching. The inset illustrates that the etching of pyramids followed by subsequent in-situ overgrowth results in a layer exhibiting tensile stress. The complete growth cycle produces a layered structure characterized by both compressive and tensile stress formation.

(figures 1(d) and (e)). The cyclically grown (001) wafers were produced using a cyclic growth time of 1.5 h followed by 2 h of oxygen etching (figure 2), with the oxygen content in hydrogen set to 2% during the etch process. The effective growth rate of the total cyclic process was 2.2 μm h^{-1}, resulting in a nitrogen-doped (001) layer with a thickness of for example 300 μm (figure 1(a)), while the growth rate for the nitrogen-doped (111) layer was only 1 μm h^{-1}. The nominally undoped layers for (111) wafers were grown with a methane content of 1.25% and a growth rate of 0.4 μm h^{-1}. These nominally undoped layers are essential as they yield better diamond quality when grown over (111) nucleation areas compared to direct growth with a nitrogen inlet flux. To achieve (111) layers with a high concentration of NV centers, these nominally undoped layers were *in-situ* overgrown with a functional nitrogen-doped layer (nitrogen content in the inlet gas mixture: 5000 ppm), through the following two CVD processes:

1. The growth process of method 5 involved 18 h of nominally undoped conditions, followed by an additional 2.5 h for the functional nitrogen-doped layer (2 μm), achieving a thickness of 9 μm on the ELO pattern of mask 1 (figure 1(d)).
2. The wafer with the stack with the masks 1 and 2 of method 6 was manufactured in several steps as follows (figure 1(e)):

The first step of method 6 was using the same recipe as in method 5. Following this, the surface was polished to prepare for the structuring of mask 2 on top of the 9 μm thick diamond layer. Subsequently, an additional 35 μm thick nominally undoped layer was grown in a process time of 89 h. (This process was once interrupted after 4 h to perform Raman and PL mappings (figure 10).) Finally, in the next growth step, the functional nitrogen-doped layer was grown for 60 h, resulting in a total diamond thickness of the stack of 100 μm. The structured Ir film of the second layer is fabricated as follows: the polished diamond surface of the (111) wafer from method 5 is coated with a 140 nm thick Ir thin film, resulting in a Ir/cC/Ir/YSZ/Si stack (figure 4(a)) and the Ir layer is structured by means of a second lithographic process with the pattern sketched in figure 3(c). A 100 nm Ni layer is deposited on top of the patterned photoresist layer with the pattern of mask 2. The Ni layer is then structured using a lift-off process. The structured Ni mask is employed to pattern the Ir mask through a dry etching process utilizing for 5 min an Ar–Cl_2–O_2 plasma at a pressure of 1.5 Pa, a RF power of 160 W and inlet flows of 35 sccm Cl, 5 sccm Ar and 10 sccm O_2 (figure 4(b)). The SEM image depicts the patterned photoresist on the Ir layer, which is used for the subsequent lift-off process (figure 5(a)). The 140 nm thick Ir film and the upper 100 nm of diamond are etched in the circular areas, where no Ni mask protects the Ir top surface, as demonstrated in the SEM image (figure 5(b)). Following this, the Ni mask is removed. EDX mapping displays the structured Ir top layer and the diamond (cC) in the etched holes (figure 5(c)). Finally, the PL map of the NV centers in the functional nitrogen-doped top layer of the diamond is visible in the holes of the Ir pattern (figure 5(d)). The Ir hard mask covers the diamond film, resulting in no PL signal from the Ir area (shown in black).

Regarding the surface structure, the diamond (001) epilayer of the standard growth gradually smoothens during the post-coalescence stage, forming flat terraces separated by steps of variable height ranging from 200 nm to 1 μm, depending on the specific growth conditions [12]. In contrast, the quadratically averaged roughness of the diamond (111) epilayer of the standard growth, measured by AFM, is only 7.5 nm.

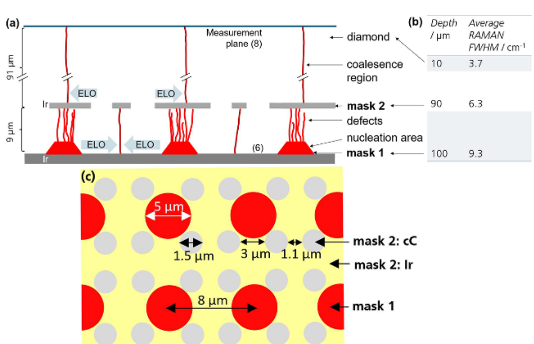

Figure 3. Schematic sketch of the concept behind the method 6, featuring a stack with two mask patterns, 1 and 2. (a) Cross-sectional view and (c) top view illustrating the two defect structure regions over the nucleation area and at the coalescence region. The suppression of these defect structures is achieved by the second structured layer (mask 2). (b) The table displays the FWHM of the Raman peak corresponding to the depth values of three measurement points, indicating an improvement in diamond quality with growth height.

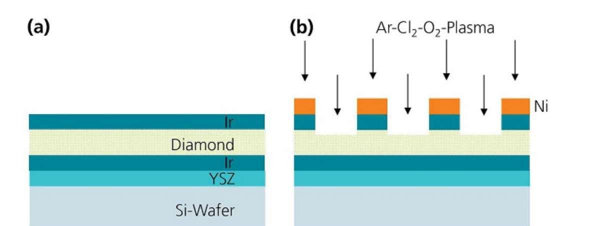

Figure 4. Manufacturing of the structured Ir layer (mask 2) of the stack of method 6. (a) The stack from method 5 was coated with a 100 nm thick Ir thin film, resulting in a Si/YSZ/Ir/cC/Ir wafer. (b) A 100 nm Ni layer was deposited on top of the mask and subsequently structured using a lift-off process. The patterned Ni mask was then employed to etch the Ir mask.

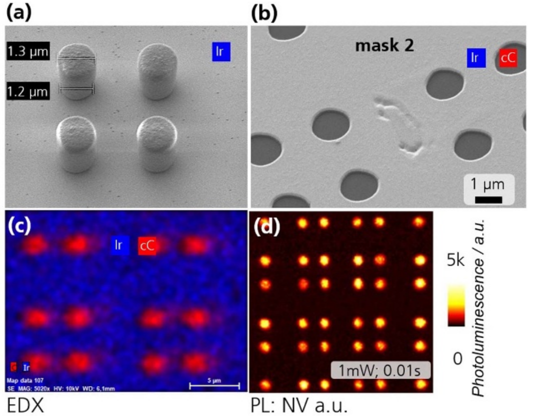

Figure 5. Manufacturing and characterization of the Ir mask 2. (a) SEM image of the patterned photoresist on top of the Ir layer. A 100 nm Ni layer was deposited onto the mask and structured using a lift-off process. (b) SEM image after etching the Ir top layer and removing the Ni layer. (c) EDX mapping illustrating the structured Ir top layer and the diamond (cC) in the etched holes. (d) Photoluminescence (PL) map of the NV centers in the functional NV top layer.

A) Method 1: Cyclic Growth

The Raman peak-shift [14] of the cyclic The Raman peak-shift [13] of the cyclic growth of method 1 is used to measure the stresses. The average tensile stress in layer (1) when overgrowing the pyramidal etch pits demonstrates the success of this process (table 2). The generally occurring compressive stresses of (001) growth are thus compensated by the tensile stress in layer (1). Layer (2) still predominantly exhibits compressive stresses. Measurements using the Raman peak-shift method in a horizontal measurement plane revealed tensile stresses of up to −0.7 GPa in areas of overgrown etch pyramids and compressive stresses of 0.6 GPa in areas without etch pyramids (figure 2). Raman measurements with numerous wafers show average full width at half maximum (FWHM) peak widths of 2.2 cm^{-1}, produced by this method 1. X-ray diffraction shows the

FWHM of the rocking curve (RC) of the diamond 004 reflection has a peak width ranging from 0.13° to 0.15°.

B) Method 2: Columnar Growth

The (001) wafers produced using the columnar growth method are freestanding and planar. However, this method has the drawback of generating opaque wafers, likely due to carbon compounds at small-angle grain boundaries between the columns. Additionally, the diamond quality is relatively low, as indicated by a FWHM of the Raman peak measuring 4.5 cm^{-1} and an RC peak width of 0.74° for the diamond 004 reflection in the x-ray diffraction. In the first step these wafers are created through an adapted biased enhanced nucleation process [12], which employs a shorter nucleation time of 10 min, compared to the standard 30 min. This reduced nucleation time leads to a nucleation structure characterized by relatively small islands. Subsequent overgrowth in ellipsoid CVD reactors results in a pyramidal diamond structure. The temperature during the CVD process is maintained below a critical limit of 750 °C to preserve the pyramidal structure and prevent its transformation into a flat diamond surface.

C) Methods 3, 4, and 5: ELO Patterns

For the patterns created on the initial Ir templates (mask 1), two designs were examined: a pixel pattern with a pitch of 8 μm and circle diameters of 5 μm (figure 6(a)), and (a) net pattern featuring horizontal and vertical lines with a pitch of 30 μm and a line thickness of 5 μm (figure 6(b)) [8, 9, 14–18]. These patterns were fabricated using lithographic processes described in [12, 19].

The patterns from methods 3, 4, and 5 exhibit systematic Raman measurement results for stress mappings, as demonstrated in figure 6. Both (001) and (111) wafers show inverse stress results in each of the two regions that are the nucleation and the lateral growth region (figures 6 (c)–(e)). The stress observed in the (001) wafers of methods 3 and 4 was dominated by the compressive stress of the nucleation regions. Evidence for this is visible in the nucleation regions of the stress mappings in figures 6(c) (yellow marker) and (d). The initial growth on these nucleation regions of (001) wafers formed 3D surface structures, as discussed in [20]. One interpretation of these overgrowth processes is that the stress in the nucleation regions is primarily influenced by coalescence phenomena of the small diamond nuclei within each circle of 5 μm diameter of the pattern [20]. An indicator pointing towards this interpretation is visible in the compressive stress at coalescence regions of two neighboring domains of the pattern after lateral overgrowth (marked by the red ellipse in figure 6(c)). We found more evidence supporting the hypothesis that the lateral overgrowth region does not dominate the stress of the (001) wafer, as the average stress in measurement plane (5) at the interface is compressive in method 3 and 4 (or more precisely, neutral in method 4), matching the stress sign of the dominant nucleation region. Conversely, in the case of (111) ELO wafers, the situation is reversed; here, the stress is dominated by overgrowing {100} facets in the lateral overgrowth region (figure 8(e)). This is attributed to the very fast transformation from the nuclei to a smooth and homogeneous thin film at less than 100 nm thickness of the nucleation regions of the (111) wafers (figure 9(e*)); while the nuclei of the (001) wafers exhibit the aforementioned 3D surface in a growth height exceeding 1 μm with a pyramidal shape (figure 9(c*)). Thus, the coalescence phenomena are mitigated in the nucleation regions of the (111) wafers of method 5, so that the stress values of the (111) nucleation regions are less dominant. This explains why the sign of the dominant stress and the average stress is the same for both (111) and (001) wafers, despite the reversed stress signs in each of the two regions: nucleation and lateral growth region. At the top surfaces in the planes (4) and (7), all patterns induced average compressive stress of both (001) and (111) oriented wafers, with results of 0.75 GPa for the (001) wafer and 1.1 GPa for the (111) wafers (table 2). The compressive stress results in a convex curvature for both wafer orientations. In the case of the (111) wafer orientation, method 5 compensates for the tensile stress that typically dominates standard-grown (111) wafers, effectively reversing the original convex curvature. Thus, the (111) wafers do not exhibit cracks (table 2). In contrast, for (001) wafers, the compensation for curvature was insufficient, leading to crack formation in (001) wafers at growth heights of less than 40 μm (figure 1(c)). Thus, methods 3 and 4 failed to invert the originally compressive stress at the wafers' top surfaces, which typically dominates standard-grown (001) wafers. A modified pixel design for the (001) wafers with larger distances between the circles could potentially overcompensate the compressive stress in the nucleation region, resulting in an average tensile stress for the first overgrowth layer. However, this new layout would lead to a more pronounced 3D top surface with a pyramidal shape, limiting the wafer's polishing capabilities. Early polishing is crucial to implement the second mask area at a growth height of less than 20 μm–40 μm, creating the next layer for stress compensation before the convex curvature becomes too pronounced. This consideration, in conjunction with our positive results from method 1, leads to our conclusion that these ELO methods with multiple mask layers are not a viable option for (001) wafer production.

Table 2. Top surface and ELO interface results of the stress and curvature analysis. No wafer cracking occurs in the two stable methods to mitigate the radius of curvature: method 1 'the cyclic growth' and method 5 'the ELO pattern'. Wafers classified as 'planar' exhibit a radius of curvature of more than 10 m and can be polished effectively. Notably, the systematic characteristics indicate that the stress sign depends solely on the overgrown {11*n*} or {100} facet that holds true across all methods without any exception.

Method	Wafer orientation	Measurement plane		Average Raman FWHM/cm^{-1}	Average stress[b]/GPa	Overgrown facet[a]	Stress sign	Wafer curvature	Result
6) ELO mask 2	(111)	8	top	3.7	1.3	{100}	−compressive	convex	crack
6) ELO mask 2	(111)	9	ELO	6.3	2.3	{100}	− compressive	convex	stable
5) ELO circle	(111)	6	top	6.3	1.1	{100}	− compressive	convex	stable
5)	(111)	7	ELO	10	3.3	{100}	− compressive	convex	stable
Standard growth	(111)	—	top	5.7	−0.4	{111}	+ tensile	concave	crack
Standard growth	(001)	—	top	2.5	0.9	{100}	− compressive	convex	crack
1) Cyclic growth	(001)	1	top (1)	2.2	−0.7	{111}	+ tensile	planar	stable
1)	(001)	2	top (2)	2.2	0.6	{100}	− compressive	planar	stable
2) Columnar	(001)	3	top	6.3	−0.05	{111}	+ tensile	planar	stable
3) ELO circle	(001)	4	top	6.0	0	{100}	neutral	convex	crack
3)	(001)	5	ELO	6.5	−0.8	{111}	+ tensile	non	crack
4) ELO net	(001)	4	top	7.4	0.75	{100}	− compressive	convex	crack
4)	(001)	5	ELO	8.3	−1.7	{111}	+ tensile	non	crack

[a]Some {111} facets might be higher indexed: {11*n*} with $n \in \mathbb{Q}^+$.

[b]In the case of the measurement planes 'ELO', each maximum stress value in the lateral overgrowth region (ELO) corresponds to its specific overgrown facet at the interface.

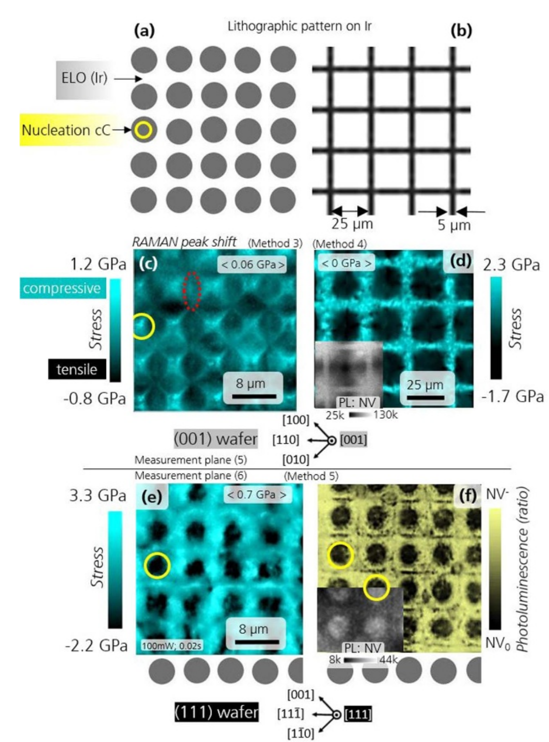

Figure 6. Analysis of stress formation in the diamond planes (5) and (6) of the nucleation and lateral growth region (ELO). (a) and (b) Schematic representations of the two lithographic patterns. (c), (d) and (e) Stress results derived from the Raman peak shift in the measurement plane directly above the Ir interface. The average stress values from the Raman maps are indicated in each diagram. The inverse stress behavior is highlighted by the yellow circles. (c) The compressive stress in the coalescence region of two neighboring domains of the pattern is marked by the red oval. (f) Photoluminescence mapping of the ratio of the NV- to NV0 signals in the spectra. (d) and (f) Insets display the mapping of the corresponding integrated PL spectra of the NV center.

The other approach to produce larger lateral overgrowth areas, using a mask with a net pattern, was applied in method 4, as already discussed (figure 6(d)). Here, the distance between the nucleation sites was increased from 3 μm (circle pattern) to 25 μm (net pattern). However, the results were inadequate, as the average stress at the interface remained dominated by the relatively small-sized nucleation areas, resulting in the average stress level of 0.0 GPa. Moreover, the net pattern intensified the curvature effects caused by compressive stress within the net area. This is due to the mechanically strong connections between all segments at the net area, leading to an even greater convex curvature compared to the not-patterned case. This finding was corroborated by testing multiple wafers (also with 45° rotated net patterns), all yielding similar results that are consistent with data from literature [8, 15]. However, we conclude that these detrimental mechanical effects on full wafer size have never been tested or demonstrated before. Consequently, our work dismisses previously proposed pattern solutions [14–16, 18] for large-scale (001) wafer production, such as the net pattern.

It is noteworthy that some standard grown (111) wafers without any ELO method did not strictly adhere to the rule of tensile stress formation at the top surface (table 2). The root cause is that the (111) wafers must be grown with a nominally undoped layer of 7 μm thickness before commencing nitrogen-doped growth to achieve optimized diamond quality. The nominally undoped and nitrogen-doped layers exhibit different stress formations, further complicating the stress characteristics. If a wafer cracked due to a low radius of curvature of less than 6 m, it is unsurprising that the stress at the top surface exhibits a more complex pattern that does not strictly adhere to the simple rules of the stress sign (table 2). However, much more relevant for the interpretations in this work is the direction of the curvature. In this regard, all wafers from all methods align with the rules outlined in table 1. Moreover, all (001) wafers and all ELO wafers align with the rule that solely the overgrown facet {100} or {111} determines the compressive or tensile stress sign, respectively. (In our work some {111} facets might be higher indexed: $\{11n\}$ with $n \in \mathbb{Q}^{+}$.)

A systematic interpretation of all ELO methods was also evident in the corresponding mappings of the FWHM of the Raman peak, where all lateral overgrowth regions showed clear signs of a significant reduction in defect density compared to the nucleation regions: the FWHM of the Raman peaks decreases substantially. Method 4, utilizing the net pattern, demonstrates a great performance in lateral defect reduction, as evidenced by the largest ELO area of approximately 20 × 20 μm^{-2} with the

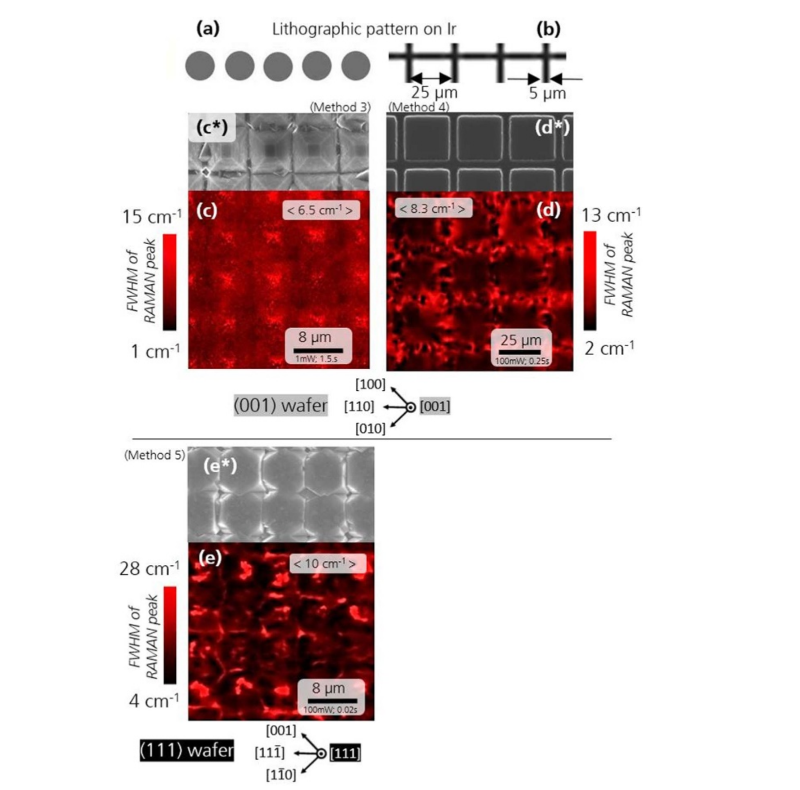

Figure 7. Analysis of material quality in the diamond planes (5) and (6) of the nucleation and lateral growth region. (a, b) Schematic representations of the two lithographic patterns. (c), (d) and (e) FWHM of the Raman peak mapping. The average FWHM values from the Raman maps are indicated in each diagram. (c*), (d*), (e*) SEM images illustrating the material structure at the interface. To enhance clarity, the process was halted after 4 h of CVD growth at a growth height of 5 μm for the two (001) wafers (c*) and (d*) and after 20 h for the (111) wafer (e*).

coherent small FWHM in the range of only 2 cm^{-1} (figure 6(d)). In the case of method 5 for the (111) wafer with the circle pattern, the FWHM shrinks by a factor of seven, from 28 cm^{-1}–4 cm^{-1}, also indicating the improvement in diamond quality. Notably, in method 5, the increased defect density at the coalescence boundary at the squared edges of each two neighboring domains of the pattern was verified (figure 7(e)). The integrated PL spectra of the NV centers shown in the insets of figures 6(d) and (f) illustrate the ELO circle and net pattern in the measurement planes (5) and (7) at the interface. The same patterns observed in the Raman measurements are evident. A relative high NV signal and, consequently, a relative high NV density are found in the nucleation regions, which is a commonly reported phenomenon [20]. The underlying reason may be a higher surface roughness during the growth process in the nucleation areas, leading to greater nitrogen incorporation compared to the smooth surfaces in the lateral overgrowth regions (ELO). The mapping of the ratio of NV^- to NV^0 signals in the PL spectra (figure 6(f)) indicates a higher relative NV^- density in the lateral overgrowth region, suggesting better material quality in that area [20]. This aligns with the results from the Raman mappings. We interpret this as evidence of the successful implementation of the ELO technique in enhancing material quality.

The following conclusion is based on the widely accepted assumption of a positive correlation between NV center concentration and nitrogen concentration. Both positive and negative correlations between relative NV concentration and compressive or tensile stress were identified in the (111) and (001) wafers: All four possible combinations were thereby observed across the two distinct ELO regions—nucleation and lateral overgrowth—accompanied by a pronounced contrast in relative NV concentration in the PL mappings (figures 8(d)–(f)). This finding implies that nitrogen incorporation cannot be considered as the mechanism behind the observed stress values.

D) Method 6: (111) Wafers with Masks 1 and 2

A limitation of the ELO methods (3, 4, and 5) for the compensation of the radius of curvature is that a single ELO pattern at the Ir interface is insufficient to compensate for the concave curvature in wafer thicknesses exceeding 20 μm. Thus, multiple mask layers with ELO patterns are necessary, which would require a polishing step for each mask layer—both costly and untested globally. In this work, we demonstrate a stack of two mask layers for (111) wafers (figure 1(e)). We implemented a second

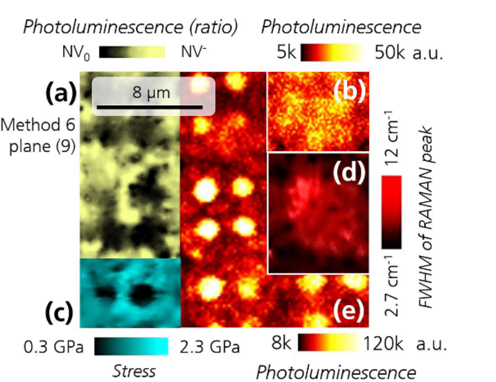

Figure 8. The growth over mask 2 of the (111) wafer was halted after 4 h CVD overgrowth to enhance clarity in the Raman and PL analysis of measurement plane (9): (a) mapping of the ratio of the NV^- to NV^0 signals of the PL spectra. (b) Integrated PL spectra. (c) Stress results derived from the Raman peak shift. (d) FWHM of the Raman peak in the same measurement plane. (e) Integrated PL spectra acquired without prior removal of the N-cap below mask 2.

mask featuring a second Ir pattern on a polished 9 μm thick (111) diamond wafer of method 5. The stack was grown to a total thickness of 10 μm. However, growth was halted at a total thickness of 70 μm to inspect the wafer for quality and crack formation. At this stage, the wafer exhibited no signs of cracking in stylus roughness measurement. During the final 30 μm of growth, however, complete-layer crack formation was observed in the diamond structure, likely due to the wafer's convex curvature (figure 1(e)). Two wafers with this stack of masks were fabricated, with the second wafer (figures 8(a)–(d)) differing in the lower nitrogen-doped layer that was removed by polishing prior to the fabrication of mask 2. This step was necessary because the NV centers of the nitrogen-doped layer would otherwise shine through the openings in the Ir layer of mask 2, artificially enhancing the apparent NV concentration in those regions. This effect is clearly visible in the integrated PL map in figure 8(e), but not in the integrated PL map with the long polished and, thus, nominally undoped diamond under the holes in figure 8(b).

The second Ir layer (mask 2) utilizes a circular pattern with circle diameters of 1.5 μm, where four circles are grouped together with a distance of 1.1 μm between them and 3 μm between groups (figure 3(c)). This design aligns with the underlying mask 1 on the same wafer (figure 3(a)). In practice, the alignment of the two masks during these initial experiments was not perfectly executed across the entire wafer area, as discussed in the following. The idea is to continue diamond growth in the high-quality lateral overgrowth areas while halting growth in the high-defect regions of the nucleation areas. This cessation of defect growth enhances the diamond quality in the overgrowth over the second Ir film, which is discussed in the following section. Additionally, there is a secondary effect that further improves diamond quality: the diamond growth over the second Ir film is an ELO step. In this overgrowth step, the FWHM of the Raman peaks decreases by a factor of more than four, from 12 cm^{-1}–2.7 cm^{-1} (figure 8(c)). This indicates that the overgrowth effects are similar to those observed over mask 1 during the first ELO step of method 5. So, the 1.5 μm diameter holes in the Ir layer can effectively be considered as the nucleation areas for the second overgrowth process.

The same systematics holds true for the stress gradient observed in measurement plane (9), directly over the Ir structure of mask 2, which resembles the stress structure observed over mask 1. The holes exhibit features akin to nucleation areas with low compressive stress of 0.3 GPa, while the lateral overgrowth regions demonstrate strong compressive stress of 2.3 GPa (figure 8(c)). Interestingly, throughout the 91 μm thick diamond layer grown over the second Ir film of mask 2, we observed compressive stress exceeding in average 1.3 GPa (table 1), with no regions of tensile stress detected. This exemplifies how effectively method 6 predetermines the stress required for the compensation of the originally concave curvature of (111) wafers. And indeed, the final radius of curvature of the (111) wafer at a thickness of 100 μm was even convex with a value of 6.5 m (table 2).

Furthermore, the diamond quality improves with growth height, as evidenced by the decreasing FWHM of the Raman peak from 9.3 cm^{-1}–6.3 cm^{-1}–3.7 cm^{-1} at depth points of 100 μm, 90 μm, and 10 μm, respectively (figure 3(b)), indicating an overall enhancement in diamond quality throughout the growth height. However, the alignment of both masks was not perfectly executed across the entire wafer area, leading to defect regions in the first diamond layer that were not mitigated by the second structured Ir layer of mask 2. Additionally, the overgrowth over the second structured layer was not conducted using an optimally refined CVD process. This is evident from the relatively high FWHM of

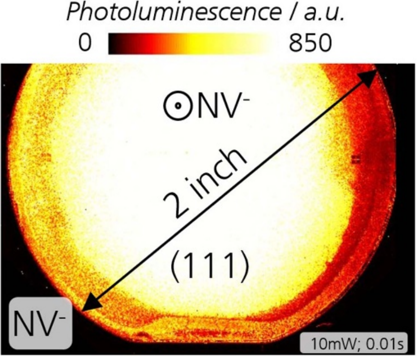

Figure 9. PL map of the peak intensity of the zero phonon line (ZPL) of the negatively charged NV center. This image demonstrates the 2 inch (111) wafer from method 5. The circular symbol denotes the orientation of the NV alignment.

the Raman peak in the regions of the holes in the Ir pattern directly over mask 2 (figure 8(d)), which is with 12 cm^{-1} nearly a factor of 2 higher than the average FWHM value at the top surface of method 5 (table 2). Thus, this FWHM result in the region of the holes in the second layer is unexpectedly high. However, this interpretation needs to be analyzed in the broader context of the extremely high stress gradient across the microscopic holes, as illustrated by the Raman mapping (figure 8(c)). The high stress gradients arise from this fine pattern with hole distances of 1.1 μm and, furthermore, from the diamond sandwich structure with the Ir layer of mask 2 situated between two diamond layers. This suggests that tensile and compressive stresses coexist at one measurement position in two orthogonal spatial directions, effectively broadening the FWHM of the Raman peak. In this consideration, the peak broadening would primarily not be caused by any defect structures. In the Raman spectra, two distinct peaks have been identified, which further supports this interpretation. In this case, the defect structure is less significant than indicated by the Raman measurement results (figure 8(d)). However, this issue extends beyond the scope of this work and should be explored further using transmission electron microscopy in future works. Therefore, in this Raman analysis, particularly focusing on the (111) stack from method (6), our additional verification of the spatial distribution of diamond quality during lateral overgrowth in measurement plane (9) through PL measurements is crucial: indeed, the mapping of the ratio of the NV^- to NV^0 signals of the PL shown in figure 8(a) supports the relative enhancement of diamond quality observed during lateral overgrowth, as discussed for method 5. This means, the NV^- ratio is higher in the lateral overgrowth region. The pattern exhibits the same structure as the holes in the Ir pattern, additionally suggesting that the holes serve as the nucleation regions for mask 2. However, these nucleation regions above mask 2 differ in that this polished diamond surface is less rough, which is reflected in the absence of an increased NV concentration within the hole area (figure 10(b)). Overall, method 6 provides evidence for the successful implementation of the ELO technique in enhancing material quality over mask 2.

ODMR analysis of the (111) wafers of method 5 and 6

In our previous work, we demonstrated the near-single alignment of NV centers through ODMR measurements [4]. Figure 9 shows the PL map of NV centers of the 2 inch wafer of method 5: The near-single alignment of the NV centers was confirmed through ODMR measurements. For comparative analysis, two ODMR spectra are provided: one for the (001) wafer (figure 10(a)) and another for the (111) wafer (figure 10(b)). This illustrates that for the (001) orientation, the NV centers exhibit four distinct orientations corresponding to four dip pairs. In contrast, the (111) orientation shows a single alignment of the NV centers that correlates with one dip pair, attributed to the self-organized NV alignment that occurs during the growth phase of the (111) wafers. Notably, the NV alignment is consistent across the entirety of the 2 inch wafer. In our previous research, we also reported ODMR results pertaining to the coherence time T_2 of 9.3 μs at the top surface of this (111) wafer [4]. Additionally, a nitrogen concentration was approximated using secondary ion mass spectrometry with the result of 7.3 ppm. An NV concentration was measured at 0.007 ppm through PL measurements. We conducted the same analysis on the (111) wafer from method 6 at the top surface over mask 2, resulting in an NV concentration of 0.01 ppm and a coherence time T_2 of 26 μs. The nitrogen concentration is estimated to be identical to that of method 5, owing to the consistent process parameters used in CVD growth and similar NV concentration results in the wafers from methods 5 and 6. Although masks 1 and 2 were not perfectly aligned, which limited the mitigation of defect structures, the coherence time T_2 was notably improved

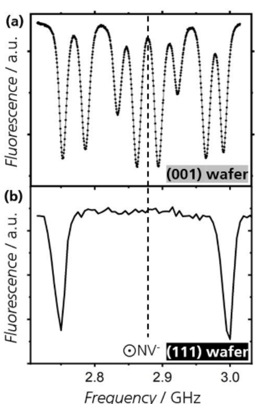

Figure 10. Continuous wave ODMR spectra acquired from the (001) and (111) wafers. The (001) wafer from method 1 exhibits a nearly equal distribution of the four orientations (a), while the (111) wafer from method 5 displays a clear dominance of one dip pair, corresponding to the single alignment of the NV center (b).

from method 5 to this initial trial of method 6, reaching the theoretical T_2 limit given its approximated nitrogen concentration [21]. The dephasing times T_2^* are determined by a Ramsey pulse sequence. While it is typically expected that T_2 exceeds T_2^* by a factor of about 5–20 [5]), the observed ratios T_2/T_2^* of about 100 for method 5 and about 235 for method 6 are already rather unusual. This behavior may be associated with strain as well as differently tilted subgrains in the heteroepitaxial material, which can affect the spin relaxation and dephasing behavior.

4. Conclusions

We found that the overgrown diamond facets {001} or {111} determine the compressive or tensile stress sign, respectively. One hypothesis for the growth mechanisms posits that there are two distinct dominating defect structures, which depend on whether the growth occurs over {001} or {111} facets. Threading dislocations tend to propagate preferentially in the <001> directions but not along the <111> directions [12], which may induce the different stress signs on the various overgrown facets. The presence of defect structures would primarily induce compressive stress on {001} facets and tensile stress on {111} facets overgrowth. A more concrete model regarding the growth mechanisms, impurity atoms and stress formation suggests that, the resulting hydrogen concentration in the grown diamond depends on the orientation of the {111} or {001} facets during the two cyclic steps of growth and annealing, with the etching process here considered as an annealing step: The distinct characteristics of the dangling bonds on the {111} and {001} facets [20, 22, 23] could lead to differing hydrogen desorption or absorption rates during annealing, or alternatively, to varying incorporation rates during growth. Here, the different gas mixtures used in the plasma during the growth and annealing steps alter the state and influence of the dangling bonds at each stage. This phenomenon is rooted in the distinct activation energies required for hydrogen transport across these facets. Verifying this hypothesis for the dependency of the hydrogen incorporation on the facet orientation is challenging due to the constant presence of hydrogen in all CVD processes. The underlying background for this hypothesis indicates that the density of incorporated hydrogen (or hydrogen complexes) in the bulk significantly influences the stress [24–27]. Thus, growth on a {111} facet or a (111) wafer surface manifests tensile stress, leading to concave curvature, and vice versa. To experimentally validate this hypothesis, quantifying the incorporated hydrogen at the diamond surface (during growth) would be necessary. However, this analysis is beyond the scope of this work. Conversely, we can exclude nitrogen incorporation as the mechanism behind the observed stress values, based on our production of a wide variety of nitrogen-doped (001) and (111) diamond wafers. This conclusion is further supported by the PL and Raman measurement results in the ELO interface regions, where both positive and negative correlations between relative NV concentration and stress sign were identified in the (111) and (001) wafers. The inversion of the stress sign and the curvature sign associated with method 6, which employs multiple mask layers, has been validated, offering great potential for stress management in (111) wafers. There is no doubt that method 6 holds immense potential for achieving an unprecedentedly low defect density on (111) wafer scale—an achievement that is highly relevant for applications in quantum computing. However, validation of this defect density is still pending. Although leaving open questions for the root cause of the induced stresses, this work proves

that any of our six growth methods controls the stress sign at the top surface, which determines the positive or negative radius of curvature. In this way the compensation of the original curvature and the growth of planarly (001) and (111) wafers on the Ir/YSZ/Si template were achieved. The fabrication of freestanding (111) wafers is pending. The 300 μm thick (001) diamond wafers with a size of 2 inch are freestanding without Si template and were double side polished.

Data availability statement

The data cannot be made publicly available upon publication because no suitable repository exists for hosting data in this field of study. The data that support the findings of this study are available upon reasonable request from the authors.

Acknowledgment

Funding under the GroDiaQ project of the German Federal Ministry of Education and Research (BMBF) is gratefully acknowledged.

Conflict of interest

The authors Engels, J. & Kustermann, J declare competing financial interests as co-inventors of a patent relevant to the subject matter of this article: Engels, J. & Kustermann, J. Patent zum Wachsen von planaren (001) Diamant-Wafern in einer Plasmakammer mit einem Wasserstoff-Methan-Gasgemisch. 167–186 (2025).

Author contributions

Jan Engels 0000-0003-3171-1190
Conceptualization (lead), Data curation (lead), Formal analysis (lead), Investigation (lead), Methodology (lead), Project administration (equal), Supervision (equal), Validation (lead), Visualization (lead), Writing – original draft (lead)

Jürgen Weippert 0000-0002-5597-5767
Data curation (equal), Formal analysis (equal), Investigation (equal), Methodology (equal), Resources (equal), Supervision (equal), Validation (equal), Writing – review & editing (equal)

Jan Kustermann
Data curation (equal), Investigation (equal), Resources (equal)

Sven Mägdefessel
Data curation (equal), Investigation (equal), Methodology (equal), Resources (equal)

Niklas Mathes
Data curation (equal), Formal analysis (equal), Investigation (equal)

Jan Jeske
Funding acquisition (equal), Project administration (equal), Resources (equal), Supervision (equal)

Lutz Kirste
Data curation (equal), Methodology (equal), Resources (equal), Supervision (equal)

Peter Knittel 0000-0002-2769-3615
Conceptualization (supporting), Funding acquisition (equal), Investigation (supporting), Project administration (equal), Supervision (equal), Writing – review & editing (supporting)

Patricia Klar
Data curation (equal), Formal analysis (equal), Investigation (equal), Methodology (equal), Resources (equal)

Tobias Fehrenbach
Investigation (equal), Methodology (equal), Resources (equal)

Christoph Wild
Conceptualization (supporting), Formal analysis (equal), Funding acquisition (equal), Investigation (equal), Methodology (equal), Project administration (equal), Resources (equal), Writing – review & editing (equal)

Vadim Lebedev
Conceptualization (equal), Data curation (supporting), Formal analysis (supporting), Funding acquisition (equal), Investigation (supporting), Project administration (equal), Resources (equal), Supervision (equal), Validation (equal), Writing – review & editing (lead)

References

[1] Michl J *et al* 2014 Perfect alignment and preferential orientation of nitrogen-vacancy centers during chemical vapor deposition diamond growth on (111) surfaces *Appl. Phys. Lett.* **104** 102407
[2] Fukui T *et al* 2014 Perfect selective alignment of nitrogen-vacancy centers in diamond *Appl. Phys. Express* **7** 55201
[3] Lesik M, Tetienne J-P, Tallaire A, Achard J, Mille V, Gicquel A, Roch J-F and Jacques V 2014 Perfect preferential orientation of nitrogen-vacancy defects in a synthetic diamond sample *Appl. Phys. Lett.* **104** 113107
[4] Weippert J *et al* 2025 Wafer scale N-doped diamond (111) with mainly nitrogen spin bath limited nitrogen vacancy coherence times from heteroepitexial growth *Phys. Status Solidi RRL* **19** 2500171
[5] Barry J F, Schloss J M, Bauch E, Turner M J, Hart C A, Pham L M and Walsworth R L 2020 Sensitivity optimization for NV-diamond magnetometry *Rev. Mod. Phys.* **92** 15004
[6] Weippert J *et al* 2023 NV-doped microstructures with preferential orientation by growth on heteroepitaxial diamond *J. Appl. Phys.* **133** 234401
[7] Mathes N, Comas M, Bleul R, Everaert K, Hermle T, Wiekhorst F, Knittel P, Sperling R A and Vidal X 2024 Nitrogen-vacancy center magnetic imaging of Fe_3O_4 nanoparticles inside the gastrointestinal tract of Drosophila melanogaster *Nanoscale Adv.* **6** 247–55
[8] Ando Y, Kamano T, Suzuki K and Sawabe A 2012 Epitaxial lateral overgrowth of diamonds on iridium by patterned nucleation and growth method *Jpn. J. Appl. Phys.* **51** 90101
[9] Ando Y and Sawabe A 2008 *Heteroepitaxy of Diamond. In Physics and Applications of CVD Diamond* ed S Koizumi, C E Nebel and M Nesladek (Wiley-VCH) pp 77–92
[10] Zhang C *et al* 2021 Diamond magnetometry and gradiometry towards subpicotesla dc field measurement *Phys. Rev. Appl.* **15** 64075
[11] Yoshikawa T, Herrling D, Meyer F, Burmeister F, Nebel C E, Ambacher O and Lebedev V 2019 Influence of substrate holder configurations on bias enhanced nucleation area for diamond heteroepitaxy: toward wafer-scale single-crystalline diamond synthesis *J. Vac. Sci. Technol. B* **37** 21207
[12] Lebedev V *et al* 2021 Growth defects in heteroepitaxial diamond *J. Appl. Phys.* **129** 165301
[13] Kato Y, Umezawa H, Teraji T and Shikata S 2011 Local stress-strain structure in CVD diamond observed by Raman peak-shift mapping *MRS Online Proc. Libr. Arch.* **1282** mrsf10–1282–a04–04
[14] Yoshikawa T, Kodama H, Kono S, Suzuki K and Sawabe A 2015 Wafer bowing control of free-standing heteroepitaxial diamond (100) films grown on Ir(100) substrates via patterned nucleation growth *Thin Solid Films* **594A** 120–8
[15] Ichikawa K, Kurone K, Kodama H, Suzuki K and Sawabe A 2019 High crystalline quality heteroepitaxial diamond using grid-patterned nucleation and growth on Ir *Diam. Relat. Mater.* **94** 92–100
[16] Ando Y, Kuwabara J, Suzuki K and Sawabe A 2004 Patterned growth of heteroepitaxial diamond *Diam. Relat. Mater.* **13** 1975–9
[17] Bauer T, Schreck M and Stritzker B 2007 Epitaxial lateral overgrowth (ELO) of homoepitaxial diamond through an iridium mesh *Diam. Relat. Mater.* **16** 711–7
[18] Washiyama S, Mita S, Suzuki K and Sawabe A 2011 Coalescence of epitaxial lateral overgrowth-diamond on stripe-patterned nucleation on Ir/MgO (001) *Appl. Phys. Express* **4** 95502
[19] Engels J *et al* 2024 High ODMR contrast and alignment of NV centers in microstructures grown on heteroepitaxial diamonds *Appl. Phys. Lett.* **124** 164001
[20] Lebedev V *et al* 2024 Coalescence as a key process in wafer-scale diamond heteroepitaxy *J. Appl. Phys.* **135** 145302
[21] Bauch E *et al* 2020 Decoherence of ensembles of nitrogen-vacancy centers in diamond *Phys. Rev. B* **102** 134210
[22] Scholze A, Schmidt W G and Bechstedt F 1996 Structure of the diamond (111) surface: single-dangling-bond versus triple-dangling-bond face *Phys. Rev. B* **53** 13725–33
[23] Scholze A, Schmidt W G and Bechstedt F 1996 Diamond (111) and (100) surface reconstructions *Thin Solid Films* **281–282** 256–9
[24] Woehrl N and Buck V 2007 Influence of hydrogen on the residual stress in nanocrystalline diamond films *Diam. Relat. Mater.* **16** 748–52
[25] Masante M *et al* 2022 Hydrogen implantation-induced blistering in diamond: toward diamond layer transfer by the Smart Cut^{TM} technique *Diam. Relat. Mater.* **125** 108913
[26] Butler J E, Thoms B D, McGonigal M, Russell J N and Pehrsson P E 1995 *Hydrogen Chemistry on Diamond Surfaces. In Wide Band Gap Electronic Materials* ed M A Prelas, P Gielisse, G Popovici, B V Spitsyn and T Stacy (Springer Netherlands) pp 105–14
[27] Hoffman A and Foord J 2011 Hydrogen interactions with diamond *Phys. Chem. Chem. Phys.* **13** 11469–70